Amorphization of silicon induced by nanodroplet impact: A molecular dynamics study

Fernan Saiz and Manuel Gamero-Castaño

Articles you may be interested in

Amorphization of silicon induced by nanodroplet impact: A molecular dynamics study

Fernan Saiz and Manuel Gamero-Castaño[a]
Department of Mechanical and Aerospace Engineering, University of California, Irvine, California 92717, USA

The hypervelocity impact of electrosprayed nanodroplets on crystalline silicon produces an amorphous layer with a thickness comparable to the droplet diameters. The phase transition is puzzling considering that amorphization has not been observed in macroscopic shock compression of silicon, the only apparent difference being the several orders of magnitude disparity between the sizes of the macroscopic and nanodroplet projectiles. This article investigates the physics of the amorphization by modeling the impact of a nanodrop on single-crystal silicon via molecular dynamics. The simulation shows that the amorphization results from the heating and subsequent melting of a thin layer of silicon surrounding the impact area, followed by an ultrafast quenching with cooling rates surpassing 10^{13} K/s. These conditions impede crystalline growth in the supercooled liquid phase, which finally undergoes a glass transition to render a disordered solid phase. The high temperature field near the impact interface is a localized effect. The significantly different temperatures and cooling rates near the surface and in the bulk explain why amorphization occurs in nanodroplet impact, while it is absent in macroscopic shock compression. Since these high temperatures and ultrafast quenching rates are likely to occur in other materials, nanodroplet impact may become a general amorphatization technique for treating the surfaces of most crystalline substrates. © *2012 American Institute of Physics*. [http://dx.doi.org/10.1063/1.4748177]

I. INTRODUCTION

Electrospraying in the cone-jet mode is an atomization technique with a singular ability for producing charged nanodroplets with narrow distributions. This technique is best known for its use in electrospray mass spectrometry.[1] It is also employed in combustion, electric propulsion, nanoparticle generation, and other applications requiring fine atomization.[2–4] An electrospray can be operated in vacuum and, when complemented with electrostatic acceleration, may be used as a source of energetic projectiles in the size range between approximately 1 nm and 1 μm. The impact of projectiles larger than 1 μm (commonly referred to as the hypervelocity impact problem) and that of atomic, molecular, and cluster ions (i.e., sizes below some 3 nm) have been studied in detail.[5,6] Conversely, the substantial intermediate size range remains largely unexplored due to the absence of projectiles, a problem that can now be resolved with the electrospray source. Recent research has shown that the impact of electrosprayed nanodroplets on materials such as silicon, silicon carbide, and boron nitride is characterized by sputtering yields (number of target atoms ejected per molecule in the projectile) of order one, and by diverse phenomena in the bombarded surface such as the appearance of craters that are orders of magnitude larger than the projectiles, extremely smooth surfaces, and amorphization.[7,8] These phenomena depend on the projectile's velocity and diameter, the projectile dose, and the nature of the target.

The impact of electrosprayed nanodroplets on single-crystal silicon is known to amorphatize a surface layer of approximately 20 nm.[8] Using drops with an average diameter of 29 nm, Gamero *et al.* have reported amorphization at projectile velocities exceeding 4.6 km/s. The interface between the amorphous and crystalline phases displays significant roughness in the scale of a few tens of nanometers, likely resulting from the discrete nature of the impacts of similarly sized projectiles. The amorphization of a region comparable in size to the projectile does not occur during the impact of macroprojectiles, which invariably leave the recovered silicon target in a polycrystalline state.[9] The simplest explanation for the observed amorphization is based on a glass transition: in this scenario, the temperature of the shocked substrate rises above its melting point T_m, which in the case of silicon has the favorable property of decreasing at increasing pressure; the neighborhood of the impact then melts and, given the small thermal diffusion time of this nanometric region, cools down at a rate that prevents the regrowth of the crystalline phase; finally the temperature of the undercooled liquid descends below the glass transition temperature forming an amorphous solid.[10] In fact similar thin amorphous layers have been obtained by melting and fast quenching of crystalline silicon during pulsed laser irradiation.[11] However appealing this amorphization mechanism does not seem to be at play during nanodroplet impact, because the temperature of shocked silicon remains well below the melting point. Instead, as the strength of the shock increases, cubic-diamond silicon undergoes a high pressure crystalline transition to its metallic beta-tin phase.[12] With this in mind, and to justify the very different outcomes of macroscopic and nano

---

[a]Author to whom correspondence should be addressed. Electronic mail: mgameroc@uci.edu.

112, 054302-1

projectile impacts, Gamero *et al.* put forward two mechanisms based on pressure-induced amorphization and the very fast pressurization and thermal transients typical of nanodroplet impact.[8] However, these explanations are hypothetical at best, and solving a first-principles model is needed to understand the physics behind the amorphization.

Molecular dynamics (MD) is a powerful technique for simulating the evolution of small systems, both in thermodynamic equilibrium as well as in non equilibrium situations. It has been used to describe the impact of larger nanoprojectiles[13,14] and that of smaller cluster and molecular ions.[15] This computational technique integrates the equations of motion of an ensemble of particles coupled by interacting potentials. The calculated positions and momenta are used to compute ensemble averages such as temperature, pressure, or density and hence to obtain the thermodynamic state of the system. In this work, we use MD to simulate the impact of a nanodroplet on a (100) Si target, modeled by the semi-empirical Stillinger-Weber (SW) potential.[16] This potential reproduces well the solid and liquid phases of silicon and predicts accurately the normal melting point, $T_m = 1690$ K versus an experimental value of 1685 K, an excellent agreement important for this study.[17] Furthermore, the SW potential has reproduced the amorphous state of silicon quenched from its melt[18] and has been used to study its undercooled liquid phases down to the final glassification.[19]

The overall goal of this article is to understand the amorphization mechanism in nanodroplet impact. Following this introduction, Sec. II outlines the simulation conditions, introduces formulae for computing thermodynamic parameters of interest, and describes the basic phenomena accompanying the impact of a 10 nm projectile. Section III shows how the projectile, impacting at a velocity of 6.4 km/s, generates an amorphous Si layer with a thickness of approximately 4 nm. The amorphization does follow a glass transition, with the unexpected melting resulting from the significant dissipation of the projectile's mechanical energy preceding the formation of a shock wave.

II. SIMULATION METHODS

We use the large-scale atomic/molecular massively parallel simulator package, LAMMPS,[20] to model the impact of a liquid droplet on a (100) Si target. The droplet has a diameter of 10 nm and is made of 1224 identical spheres distributed in a hexagonal close-packed arrangement. Each sphere has a radius of 0.422 nm, a mass of 391.31 amu, and represents a molecule of the ionic liquid 1-ethyl-3-methylimidazolium bis (trifluoro-methylsulfonyl) imide, $C_8H_{11}F_6N_3O_4S_2$, used in the nanodroplet impact research of Ref. 8. The target is a slab 30.55 nm in the impact direction (y), 48.88 nm $\times$ 48.88 nm wide in the lateral directions (x and z), and is filled with 4 390 200 Si atoms in the standard cubic-diamond arrangement. The impact direction is aligned with the [100] direction of the crystal. The interactions between liquid molecules and between liquid molecules and silicon atoms are modeled with a Ziegler-Biersack-Littmark two-body potential,[21] frequently used in impact problems of dissimilar materials:[22–24]

$$U(r) = \frac{Z_1 Z_2}{r} \varphi(r), \tag{1}$$

where Z_1 and Z_2 are the atomic number of the sphere (198, computed as the sum of the atomic numbers of its atomic constituents) and silicon, r is the interatomic distance between two particles, and $\varphi(r)$ is the empirical screening potential function

$$\varphi(r) = \sum_{i=1}^{4} a_i e^{-b_i r / a_U}, \tag{2}$$

with coefficients $a_1 = 0.1818$, $a_2 = 0.5099$, $a_3 = 0.2802$, $a_4 = 0.02817$, $b_1 = 3.2$, $b_2 = 0.9423$, $b_3 = 0.4028$, $b_4 = 0.201$.[21] a_U is defined as

$$a_U = \frac{0.854 a_B}{Z_1^{0.23} + Z_2^{0.23}}, \tag{3}$$

where a_B is the Bohr radius (0.539177 Å). The cutoff distance for the interactions between molecule-molecule and silicon-molecule is set to 0.803 nm, i.e., at 95% of the diameter of the ionic liquid molecule. The usual parametrization of the SW potential is used for the interaction between silicon atoms.[16]

The droplet is directed towards the target with an initial velocity of 6.4 km/s and a temperature of 0 K. At this velocity, the stagnation pressure and the kinetic energy per molecule are 31.33 GPa and 81.82 eV. The faces of the slab in the y direction are two free surfaces, while periodic boundary conditions are imposed in the x and z directions. All faces of the slab except for the top free surface are in contact with a Berendsen thermostat at 293 K, to help prevent the reflection of shock waves arriving at the domain boundaries.[25] The simulation uses a 1 fs integration time step and is run for 70 ps. By the time, the simulation is stopped the dynamic phenomena produced by the impact have died out, and the temperature field of the slab is almost uniform and near the temperature of the thermostat.

Figure 1 shows silicon atoms and liquid molecules in a slice bounded by planes z = −0.5 nm and z = 0.5nm, at different times of the simulation. Silicon atoms with a potential energy higher than −4.10 eV are displayed in blue, while those with lower values are shown in red. Since the average atomic potential energy for the cubic-diamond phase is −4.29 eV, the blue areas are indicative of atomic arrangements that significantly depart from the crystalline structure. In fact, the average potential energy for the amorphous phase is −4.10 eV,[18] and therefore blue is indicative of highly disordered, maybe even amorphous configurations. The frames show how the projectile penetrates the target, carving a crater with a maximum volume at about 5 ps. The surface of the crater then contracts and expands several times, relaxing to a final volume with a depth of 9.8 nm and a maximum width of 7.1 nm. A number of Si atoms are ejected from the slab.

The temperature at the position of an atom j is computed by the usual average of the kinetic energies of neighboring atoms
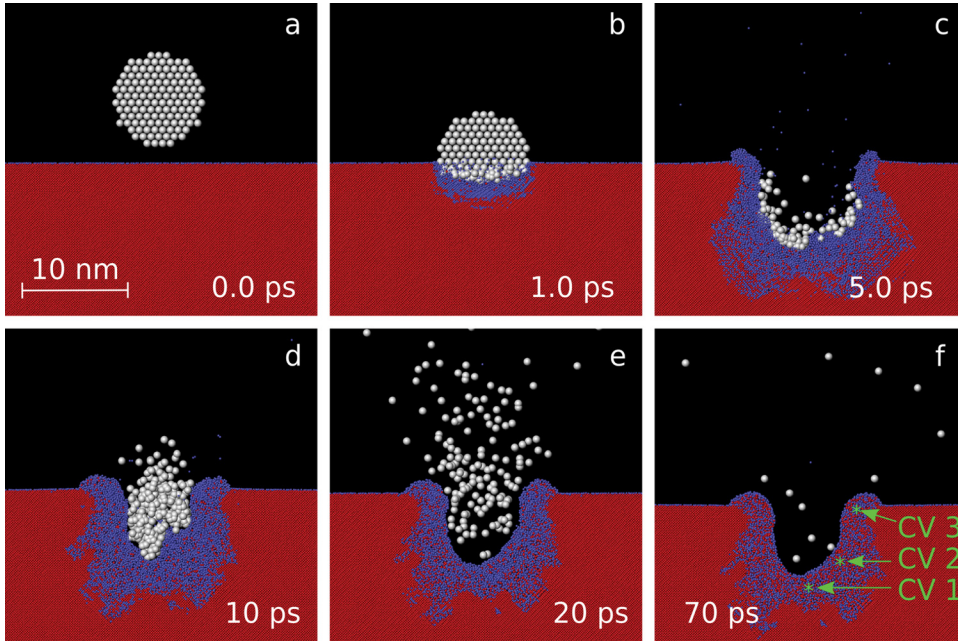
FIG. 1. Cross-sectional images of the impact at 0 ps, 1 ps, 5 ps, 10 ps, 20 ps, and 70 ps. White spheres represent the molecules of the projectile, while silicon atoms are depicted in blue or red depending on whether their potential energies are higher or lower than −4.10 eV.

$$T(\mathbf{x}^j) = \frac{m \sum_{i=1}^{N} (\mathbf{v}^i - \langle \mathbf{v}^i \rangle) \cdot (\mathbf{v}^i - \langle \mathbf{v}^i \rangle)}{2 k_B N},$$

$$\|\mathbf{x}^i - \mathbf{x}^j\| \leq 1.08 \text{ nm}, \tag{4}$$

where k_B is the Boltzmann's constant, m is the mass of a silicon atom, and $\mathbf{x}$ and $\mathbf{v}$ are the position and velocity vectors of individual atoms. All N atoms within a spherical control volume with a radius of 1.08 nm and centered in atom j are included in the average. Typically, there are some 280 atoms inside the control volume, a sufficient number to obtain reliable statistics. We have also confirmed that, with the exception of atoms near the moving shock wave generated by the impact, the velocity distributions inside these control volumes do not depart significantly from a Maxwellian, and therefore it is a good approximation to consider that the atoms in the slab are in partial equilibrium. Figure 2 shows

the temperature field in the slab for the frames in Fig. 1. Upon impact, a substantial amount of energy is dissipated in the contact region, raising its temperature above several thousand degrees (see 5 ps frame). This evolving layer surrounding the crater remains above the normal melting point for over 10 ps, before cooling down and equilibrating with its surroundings.

The virial stress for a single atom j is computed by the formula

$$\sigma_{\alpha\beta}^j = m v_\alpha^j v_\beta^j + \frac{1}{2} \sum_{i \neq j} \left(-\frac{1}{r} \frac{\partial U}{\partial r} \right) r_\alpha r_\beta \big|_{r=r_{ji}}, \tag{5}$$

where α and β refer to the x, y, and z Cartesian coordinates. The summation is done over all atoms inside the range of the potential. Similarly to the temperature, we define the stress at the position of atom j as the average of the virial stresses of all atoms within a spherical control volume centered in atom j, divided by the volume of the sphere.[14] Figure 3
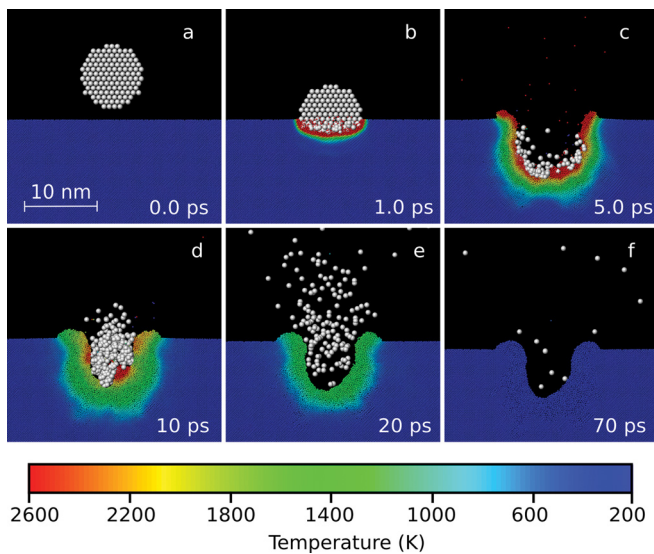

FIG. 2. Temperature field in the slab at 0 ps, 1 ps, 5 ps, 10 ps, 20 ps, and 70 ps. The temperature in an area surrounding the impact remains above the melting point for over 10 ps.
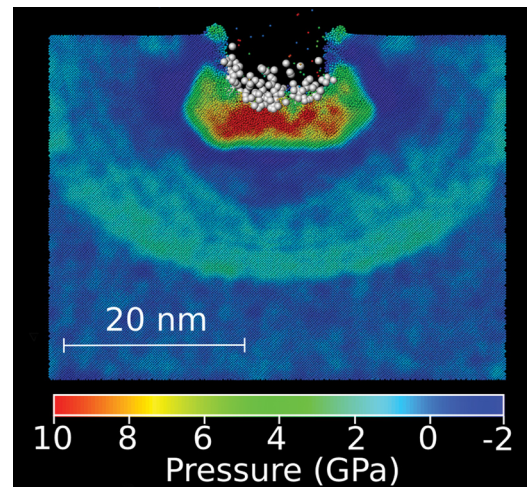

FIG. 3. Pressure field at 3.5 ps. A shock wave moves away from the point of impact at a speed of 8.31 km/s. The front at the axis of impact is located 26 nm below the surface.

shows the pressure field in the slab at 3.5 ps. The area at the bottom of the crater is decelerating the projectile and therefore is highly compressed, while a nearly spherical elastic wave moves away from the point of impact. The velocity of the front along the axis of impact is 8.31 km/s, slightly below the experimental sound speed in the [100] direction (8.43 km/s at room temperature and 1 atm). Although not shown in this figure the jump in temperature across the shock wave averages to 9 K, a marginal increase consistent with the nearly isentropic nature of shock compression.

Figure 4 shows the evolution of the total thermal, translational, and potential energies of the slab, and the total kinetic energy of the projectile, $E_{Th}(t)$, $E_{CM}(t)$, $E_P(t)$, and $E_K(t)$, respectively. They are computed by adding the respective energies of all atoms in the slab and in the projectile; the thermal energy of an atom j is $k_B T(\mathbf{x}^j)$, where the temperature is defined by Eq. (4). The average velocities of the 1.08 nm spherical control volumes are used to compute the translational energy. To illustrate better how the energy is transferred to the slab the thermal, translational, and potential energies are offset by their initial values preceding the impact, and normalized by the initial projectile's energy (1.03×10^5 eV). The projectile molecules lose 90% of their initial kinetic energy within 3 ps. By this time, 12%, 18%, and 60% of the projectile's energy has been transferred to the slab in the form of translational, thermal and potential energies, respectively. After peaking at 12 ps, the thermal energy in the slab is gradually lost by heat conduction with the surrounding thermal bath, while the potential energy asymptotes to a constant fraction of 24%. This potential energy excess is mostly distributed in the region near the impact, where the atomic arrangement is highly disordered by the end of the simulation.

III. AMORPHIZATION MECHANISM

Figure 1(f) shows the centers of three control volumes with radii of 1.08 nm, at the end of the simulation. The control volumes are located near the crater surface, in the layer where the atomic structure clearly departs from the crystal-
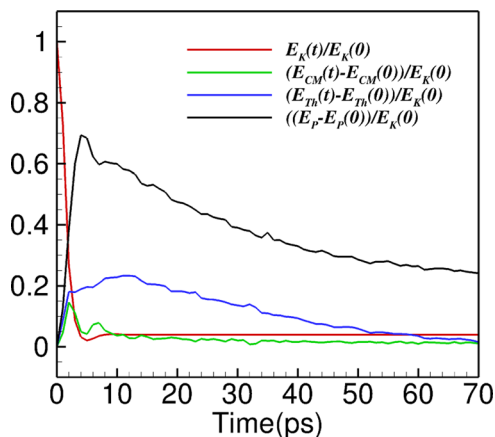
TABLE I. Thermodynamic and structural information near the point of impact at 70 ps (CV1, CV2 and CV3). T, P_E, ρ, CN, $\langle\theta\rangle$ and $\sigma(\theta)$ stand for temperature, average potential energy, density, average coordination number, average bond angle and standard deviation of the bond angles. a-Si (SW) and g-Si (SW) are amorphous and glassy phases of silicon from molecular dynamics simulations using the Stillinger-Weber potential,[18] a-Si (exp) is for a vapor deposition sample,[23] and c-Si (SW) is for the crystalline phase in the slab before the impact.

Sample	T(K)	P_E(eV)	ρ(kg/m^3)	CN	$\langle\theta\rangle$(deg)	$\sigma(\theta)$(deg)
CV1	376	−4.04	2439	4.49	107.5	19.3
CV2	355	−4.06	2482	4.63	106.5	20.8
CV3	395	−4.05	2456	4.45	107.2	19.6
a-Si (SW)	300	–	2345	4.21	107.8	16.0
g-Si (SW)	300	−4.10	2477.25	4.66	106.6	22.6
a-Si (exp)	300	–	2395.67	3.95	–	–
c-Si (SW)	288	−4.30	2413	4	109.5	2.9

line arrangement. We will compute several parameters for each control volume to prove that a disordered, non-crystalline phase results from the impact. Table I collects the average potential energy, density, average coordination number, and the average and standard deviation of the bond angle distribution of each control volume. These parameters are good indicators of the thermodynamic state and allow a comparison with published values of disordered and crystalline Si phases, also listed in the Table I. The experimental amorphous phase, a-Si (exp), is a sample obtained by vapor deposition.[26] The data referred to as a-Si (SW) and g-Si (SW) are for amorphous and glassy phases resulting from fast quenching at different cooling rates and obtained via molecular dynamics using the Stillinger-Weber potential.[18] Further structural information is given in Fig. 5 in the form of radial distribution functions. As can be seen in Table I, and especially in Fig. 5, the control volumes near the area of impact are in a disordered state nearly identical to the glassy g-Si (SW) phase. Although clearly non-crystalline, it was early recognized that the structure of g-Si (SW) differed from that of amorphous silicon in its higher average coordination number, and the appearance of a near-side shoulder on the second peak of the radial distribution (see shoulder at 0.33 nm in the

FIG. 4. Total thermal (E_{Th}), translational (E_{CM}) and potential (E_P) energies of the slab, and total kinetic energy of the projectile (E_K), as functions of time. The thermal, translational, and potential energies are offset by their initial values preceding the impact, and normalized by the initial projectile's energy (1.03×10^5 eV).
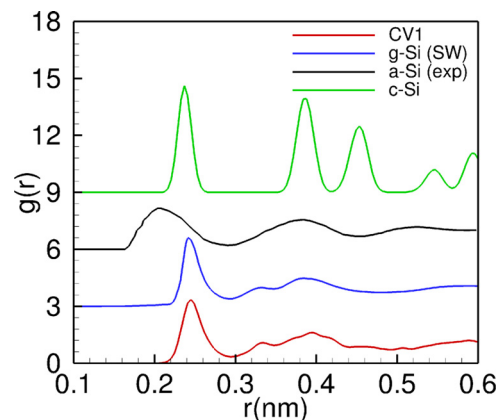

FIG. 5. Radial distribution functions for the atoms in control volume CV1, the glassy state g-Si (SW), the amorphous phase a-Si (exp), and crystalline silicon.

CV1 and g-Si (SW) curves in Fig. 5). Although this disagreement was initially explained in terms of the inadequacy of the SW potential for reproducing the glass transition of silicon, Luedtke and Landman found that it was rooted on kinetics since they were able to obtain a-Si (SW), with properties nearly identical to experimental amorphous phase, by enforcing a slower cooling rate (approximately 2×10^{11} K/s). In the paragraph below we show that the undercooled liquid phase resulting from the impact is quenched at rates exceeding 10^{13} K/s, and therefore it is not surprising that the final solid is in the glassy g-Si (SW) state.

We next follow the trajectory of the central atom in control volume CV1 and quantify the thermodynamic state of the neighborhood of this moving atom to identify the mechanism responsible for the overall crystalline to amorphous phase transition. Figure 6 shows the evolution of the temperature, pressure, and coordination number of the moving control volume. It also displays a melting point curve, which is a function of the hydrostatic pressure, $T_m(P_H)$.[27] Although the pressure in the slab is not hydrostatic we will use its value to estimate the melting point. The center of the control volume is initially 7.72 nm below the free surface, and it takes 1.0 ps for changes associated with the impact to reach this position. At this time, the pressure and the temperature start to increase, and rapidly plateau around 5.2 GPa and 350 K at 1.8 ps. During this initial compression, the material remains in the cubic-diamond arrangement, as seen from its constant coordination number of 4. Additional confirmation is provided by the radial distribution function at 1.8 ps in Fig. 7, which has the isolated peaks of the crystalline arrangement.
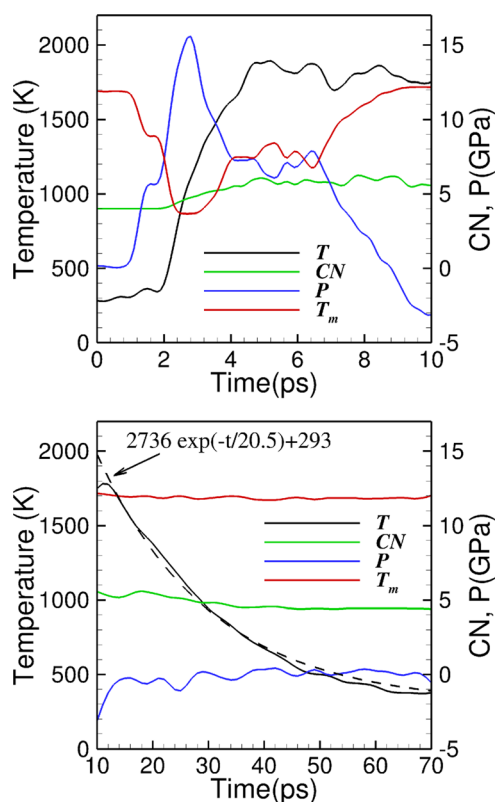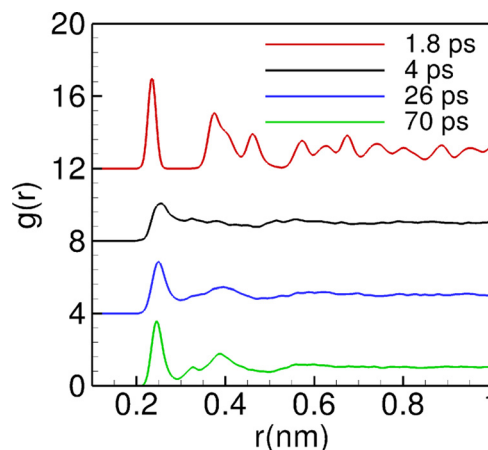

FIG. 7. Radial distribution functions for the atoms in control volume CV1 at 1.8 ps, 4 ps, 26 ps, and 70 ps.

This initial phase is followed by a sustained increase of the temperature, pressure, and coordination number. At about 2.2 ps, the temperature exceeds the melting point, and the control volume starts to undergo a solid to liquid phase transition. This is confirmed by the coordination number fluctuating around a value of 6 and the disappearance of long-range order in the radial distribution function at 4.0 ps. Although not shown in these figures the simulation captures other signs typical of the liquid phase such as the almost complete elimination of shear stresses, and the near hydraulic nature of the pressure. It is worth noting that although the pressure peaks at 15 GPa around 2.3 ps and rapidly decays afterward, the temperature does not reach its maximum value of 1900 K until approximately 8 ps, once the control volume is largely unloaded. From this point on the temperature decays at a rate well fitted by the exponential law $T(K) = 2736 \, \mathrm{Exp}(-t(ps)/20.5) + 293$. The cooling rates are as high as 6.8×10^{13} K/s at the normal melting point and 3.7×10^{13} K/s at the glass transition temperature of 1060 K.[19] It is worth noting that these cooling rates exceed by over four orders of magnitude the typical value of 10^9 K/s needed to prevent the regrowth of the crystalline phase.[11] As the control volume cools down the second coordination shell at 0.4 nm begins to develop (see radial distribution function at 26 ps, $T = 1060$ K), signaling the onset of glassification. Finally at 70 ps and a temperature of 376 K, the second coordination shell is well resolved, while all other long range peaks remain suppressed, and the radial distribution curve is identical to that of the glassy g-Si (SW) phase.

Although the hypervelocity impacts of a nanodroplet and macroscopic projectiles are similar problems, it is apparent that the steady shock wave theory commonly used to interpret the latter cannot predict the observed amorphization: the temperature increases only modestly behind a steady shock front, e.g., as low as a few tens of degrees for a pressurization of 15 GPa in silicon,[28] which is clearly insufficient to melt the solid phase. Figures 3 and 4 offer clues to the unexpected difference. Figure 3 shows how the impact does generate a shock wave, which is fully developed by the time it travels 26 nm into the slab. The changes in thermodynamic variables, particle velocity, and stress across the shock

FIG. 6. Temperature, coordination number, pressure, and melting point in the control volume CV1 as functions of time.

are consistent with those for an elastic wave. On the other hand, it is apparent that near the impact the standard jump conditions across a steady shock cannot be fulfilled because basic assumptions such as the homogeneity of the material and the existence of a shock wave travelling at constant speed break down. It appears that there is an initial zone in the substrate where the non uniform momentum exchange between projectile molecules and silicon atoms is homogenized, setting up the conditions required for the development of the steady shock wave. Figure 4 indicates that this homogenization is accompanied by the dissipation of approximately 23% of the projectile's kinetic energy into thermal energy, which is ultimately responsible for the melting of the crystal.

In summary, the simulation shows that upon impact of a 10 nm projectile 23% of its kinetic energy is dissipated into the silicon slab near the point of contact, melting a layer with a thickness of a few nanometers. This layer then cools down at rates exceeding 10^{13} K/s, far surpassing the typical value of 10^9 K/s known to prevent recrystallization. Under such quenching conditions, the undercooled liquid must solidify as an amorphous phase, regardless of whether the fast kinetics prevent the Stillinger-Weber potential from reproducing a physical amorphous phase. The high dissipation of kinetic energy within a short distance from the impact and the ultrafast quenching phenomena are not restricted to silicon substrates, and therefore this technique should be able to amorphize thin surface layers in other crystalline materials having lower or similar melting points, under cold bulk conditions.

ACKNOWLEDGMENTS

[1] J. B. Fenn, M. Mann, C. K. Meng, S. K. Wong, and C. M. Whitehouse, Science **246**, 64 (1989).

[2] I. G. Loscertales, A. Barrero, I. Guerrero, R. Cortijo, M. Marquez, and A. M. Gañán-Calvo, Science **295**, 1695 (2002).

[3] D. C. Kyritsis, S. Roychoudhury, C. S. McEnally, L. D. Pfefferle, and A. Gomez, Exp. Thermal Fluid Sci. **28**, 763 (2004).

[4] M. Gamero-Castaño, J. Propul. Power **20**, 736 (2004).

[5] I. Yamada and N. Toyoda, Surf. Coat. Technol. **201**, 8579 (2007).

[6] L. D. Libersky, A. G. Petschek, T. C. Carney, J. R. Hipp, and F. A. Allahdadi, J. Comput. Phys. **109**, 67 (1993).

[7] M. Gamero-Castaño and M. Mahadevan, J. Appl. Phys. **106**, 054305 (2009).

[8] M. Gamero Castaño, A. Torrents, L. Valdevit, and J.-G. Zheng, Phys. Rev. Lett. **105**, 145701 (2010).

[9] H. Kishimura and H. Matsumoto, J. Appl. Phys. **103**, 023505 (2008).

[10] D. Turnbull, Contemp. Phys. **10**, 473 (1969).

[11] M. O. Thompson, J. W. Mayer, A. G. Cullis, H. C. Webber, N. G. Chewet, J. M. Poate, and D. C. Jacobson, Phys. Rev. Lett. **50**, 896 (1983).

[12] D. C. Swift, G. J. Ackland, A. Hauer, and G. A. Kyrala, Phys. Rev. B **64**, 214107 (2001).

[13] J. Samela and K. Nordlund, Phys. Rev. Lett. **101**, 027601 (2008).

[14] P. S. Branicio, R. K. Kalia, A. Nakanoa, P. Vashishta, F. Shimojo, and J. P. Rinob, J. Mech. Phys. Solids **56**, 1955 (2008).

[15] N. Winograd, Z. Postawa, J. Cheng, C. Szakal, J. Kozole, and B. J. Garrison, Appl. Surf. Sci. **252**, 6836 (2006).

[16] F. H. Stillinger and T. A. Weber, Phys. Rev. B **31**, 5262 (1985).

[17] J. Q. Broughton and X. P. Li, Phys. Rev. B **35**, 9120 (1987).

[18] W. D. Luedtke and U. Landman, Phys. Rev. B **40**, 1164 (1989).

[19] S. Sastry and C. A. Angell, Nature Mater. **2**, 739 (2003).

[20] S. J. Plimpton, J. Comput. Phys. **117**, 1 (1995).

[21] J. F. Ziegler, J. P. Biersack, and U. Littmark, *The Stopping and Range of Ions in Solids* (Pergamon, New York, 1985).

[22] S. Valkealahti and R. M. Nieminen, Nucl. Instrum. Methods B **18**, 365 (1986).

[23] E. Holmström, J. Samela, and K. Nordlund, Europhys. Lett. **96**, 16005 (2011).

[24] T. Aoki, T. Seki, S. Ninomiya, and J. Matsuo, Surf. Coat. Technol. **201**, 8427 (2007).

[25] J. Samela, J. Kotakoski, K. Nordlund, and J. Keinonen, Nucl. Instrum. Methods B, **239**, 331 (2005).

[26] P. Evans, G. Devaud, T. Kelly, and Y.-W. Kim, Acta Metall. Mater. **38**, 719 (1990).

[27] E. G. Ponyatovsky and O. I. Barkalov, Mater. Sci. Rep. **8**, 147 (1992).

[28] S. D. Gilev and A. M. Trubachev, J. Phys.: Condens. Matter **16**, 8139 (2004).